Optical properties of CuCl microcavities with fluctuations in their refractive index profiles along the cavity structures

S. Yoshino,[1] G. Oohata,[1] Y. Shim,[2] H. Ishihara,[2] and K. Mizoguchi[1]

[1]*Department of Physical Science, Graduate School of Science, Osaka Prefecture University, 1-1 Gakuen-cho, Naka-ku, Sakai 599-8531, Japan*

[2]*Department of Physics and Electronics, Graduate School of Engineering, Osaka Prefecture University, 1-1 Gakuen-cho, Naka-ku, Sakai 599-8531, Japan*

(Received 5 June 2013; revised manuscript received 7 November 2013; published 25 November 2013)

We report on the optical properties of the CuCl microcavities that exhibit fluctuations in their refractive index profiles along the cavity structures. The angle-resolved reflectance spectra of the CuCl microcavities with a cavity length of half-integer multiples for the Z_3 exciton wavelength clearly show three cavity-polariton modes and minor modes. The Rabi splitting energies observed in the cavity-polariton modes are widely controlled by changing the cavity length of the microcavity. To analyze the spectral profile and the Rabi splitting energies qualitatively, the refractive index profiles of the constituent layers in the CuCl microcavities are evaluated using spectroscopic ellipsometry, and the reflectance spectra of the CuCl microcavities with the fluctuations in the refractive index profiles of the microcavity structures are calculated using the nonlocal response theory. The calculated reflectance spectra reproduce very well the cavity-polariton modes and the minor modes, including their energies and spectral profiles, in the observed reflectance spectra, which indicates an essential role of the fluctuation effect of the refractive indices of constituent layers in controlling the Rabi splitting energies and the quality factor of the microcavity.

DOI: 10.1103/PhysRevB.88.205311 PACS number(s): 78.67.Pt, 71.36.+c, 71.35.−y

I. INTRODUCTION

In semiconductor microcavities, the strong exciton-photon coupling states form new eigenstates that are referred to as cavity polaritons. The cavity polariton has many interesting behaviors, including a peculiar energy-dispersion relationship, light effective mass, and a bosonic nature, due to the coupling between photons and excitons. These properties enable many types of new physical phenomena. The cavity polaritons in semiconductor GaAs quantum-well (QW) microcavities were demonstrated by Weisbuch *et al*. for the first time.[1] III-V semiconductor microcavities are reflected in many polaritonic phenomena, such as the polariton Bose-Einstein condensation,[2,3] a parametric amplifier,[4] and polariton lasing[5] for many-body quantum coherence phenomena, and the Jaynes-Cummings ladder[6] for single polaritonic phenomena.

Recently, wide-band-gap semiconductor microcavities, such as those of ZnO and GaN,[7–10] have been reported. Their large exciton binding energies and oscillator strengths can produce stable polariton states at high temperatures. In addition, large mode splitting called vacuum Rabi splitting can also occur. Moreover, the nonlinear optical response is enhanced in the microcavity system with stable excitons and biexcitons.[11] Notably, the semiconductor CuCl microcavity exhibits large Rabi splitting energies due to the large binding energy and oscillator strength of the excitons.[12] The nonlocal optical response theory for the CuCl microcavity predicts a highly efficient generation of the entangled photon pair, which is one of the nonlinear optical properties of this microcavity.[13–15] To achieve the highly efficient generation of the entangled photon pair, it is essential to control the Rabi splitting energy and the dispersion relationship of the cavity polariton. Nakayama *et al*. demonstrated controlling the Rabi splitting energies from 22 (37) to 71 (124) meV for the Z_3 ($Z_{1,2}$) exciton by changing the active-layer thickness in the region that is less than half of the effective length for the resonant wavelength of the Z_3 exciton.[16] In the region that is more than half of the effective length, Oohata *et al*. determined the optical properties of the CuCl microcavity by comparing the angle-resolved reflectance and theoretical spectra.[12] The theoretical reflectance spectra have been calculated using the nonlocal response theory. The nonlocal response theory is appropriate for a quantitative analysis of the spectral profiles and the Rabi splitting energies of the microcavities, because this theory accurately utilizes the electric field variation in the coherent region of the exciton wave function. Unfortunately, the calculated and experimental spectra reported in Ref. 12 were not in agreement quantitatively, and the origin of the disagreement was not revealed. To reveal the origin of the disagreement is one of the important subjects to control the Rabi splitting energies and derive novel optical responses in the wide-band-gap semiconductor microcavities. We expect that the disagreement between the calculated and experimental spectra will originate from the imperfections of the spatial structures in the microcavities. The imperfections cause the fluctuations in the refractive index profiles along the cavity structures, and thus the observed optical spectra in the fabricated microcavities will deviate from the expected ones in the ideally designed microcavities. To analyze the spectral profiles and the Rabi splitting energies of the CuCl microcavities quantitatively, it is necessary to clarify the effect of the spatial fluctuations in the refractive index profiles on the microcavity optical properties. Here, we demonstrate the calculated reflectance spectra of the CuCl microcavities using the nonlocal response theory and taking account of the fluctuation in the refractive index profiles of the microcavity structures.

The CuCl microcavities were fabricated with distributed Bragg reflectors (DBRs) consisting of $PbCl_2$/NaF multilayers. The observed angle-resolved reflectance spectra in

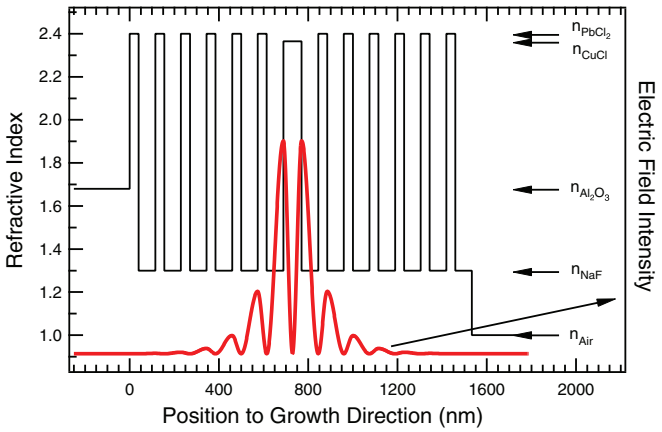

FIG. 1. (Color online) Refractive index profile of the ideal cavity structure in the CuCl λ cavity embedded in the $PbCl_2$/NaF DBRs (black thin line) and the calculated intensity profile of the electric field in the CuCl λ cavity at the normal incidence, using a transfer-matrix method (red thick line). n_A indicates the refractive index of a layer A.

the microcavities with varying active-layer thickness show the cavity-polariton and minor modes in the region of the active-layer thickness that is more than half of the effective length for the resonant wavelength of the Z_3 exciton. This indicates that the Rabi splitting energies can be controlled by simply changing the active-layer thickness. Moreover, to clarify the fluctuations in the refractive index profiles of the microcavity structures, the refractive index profiles of the constituent layers in the microcavities have been characterized using spectroscopic ellipsometry. The reflectance spectra of the CuCl microcavities with the evaluated refractive index profiles are calculated using the nonlocal response theory, and they have been compared with the observed reflectance spectra. Observing this comparison, we discuss how the effect of the spatial fluctuation in refractive indices plays a role in determining the spectral profiles and the Rabi splitting energies.

II. EXPERIMENT AND ANALYSIS

CuCl microcavities with DBRs on (001) Al_2O_3 substrates were grown using the vacuum deposition method. In this work, $PbCl_2$ and NaF were used as the constituent layers of the DBRs because the contrast of the refractive index between $PbCl_2$ and NaF layers ($n_{PbCl_2} = 2.4$ and $n_{NaF} = 1.3$ at 3.2 eV) was sufficiently high. Therefore, we expect that the $PbCl_2$/NaF DBRs will show a high reflectivity and a wide stop band. In an empty cavity containing the $PbCl_2$/NaF DBRs, the quality (Q) factor, which was estimated from an empty cavity transmission spectrum, was approximately 250. This was higher than that of the $PbBr_2/PbF_2$ DBR.[12] The CuCl microcavity was comprised of a CuCl active layer sandwiched between a top DBR with 6.5 periods and a bottom DBR with 6 periods. The active-layer thickness, called the cavity length L_{cav}, was designed to have half-integer multiples of the effective length λ: $L_{cav} = m\lambda/2$. λ is given by λ_{ex}/n_b, where λ_{ex} is the resonant wavelength of the Z_3 exciton in vacuum ($\lambda_{ex} = 387$ nm), n_b is the background refractive index, and m is an integer. Hereafter, we refer to a CuCl microcavity with $L_{cav} = m\lambda/2$ as the

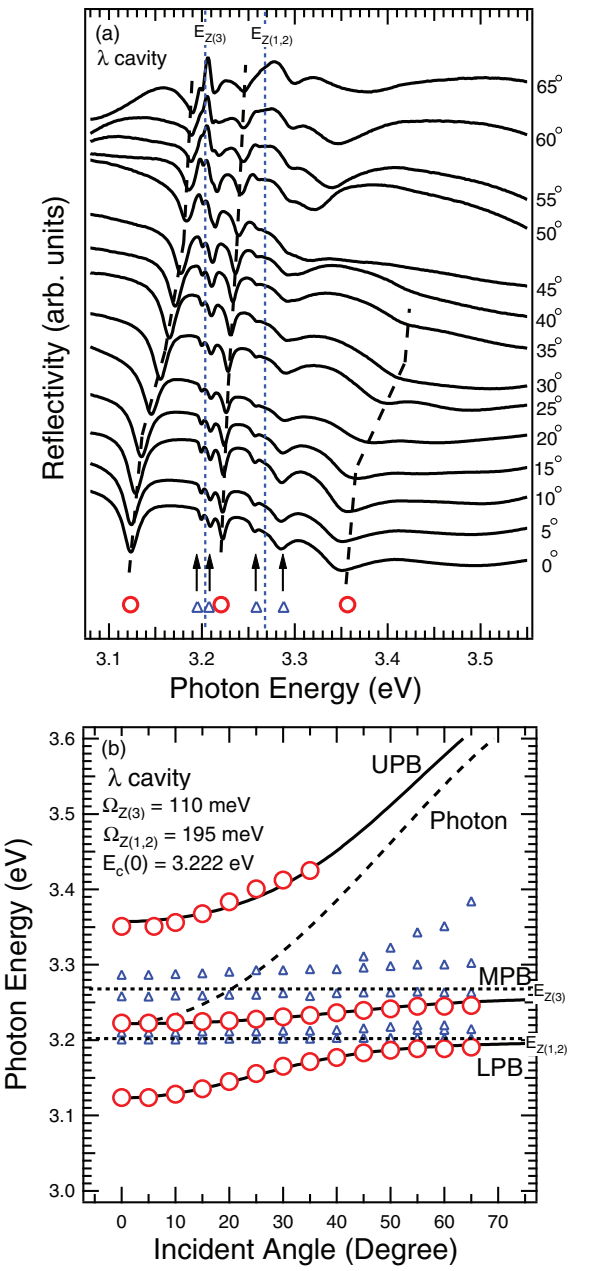

FIG. 2. (Color online) (a) Angle-resolved reflectance spectra of the CuCl λ cavity at 13 K. Open circles and open triangles indicate the strongly coupled modes and weakly coupled modes, respectively. The vertical dotted lines show the energy positions of the Z_3 and the $Z_{1,2}$ excitons of CuCl. The dashed lines are guides for the eye. (b) Variations of the dip energies of the cavity polaritons as a function of incident angle obtained in the angle-resolved reflectance spectra. The open circles and triangles are the energy positions of the strongly coupled modes and weakly coupled modes, respectively. The solid lines are the dispersion relationships of the cavity-polariton modes of the LPB, MPB, and UPB calculated from Eq. (2). The dotted lines indicate the Z_3 ($Z_{1,2}$) exciton energies, and the dashed curve shows the dispersion relationship of the cavity photon.

"$m\lambda/2$ cavity." The thicknesses of the $PbCl_2$ and NaF layer were designed to be $\lambda/4$. The difference in thickness between the fabricated and designed DBRs with one period, estimated

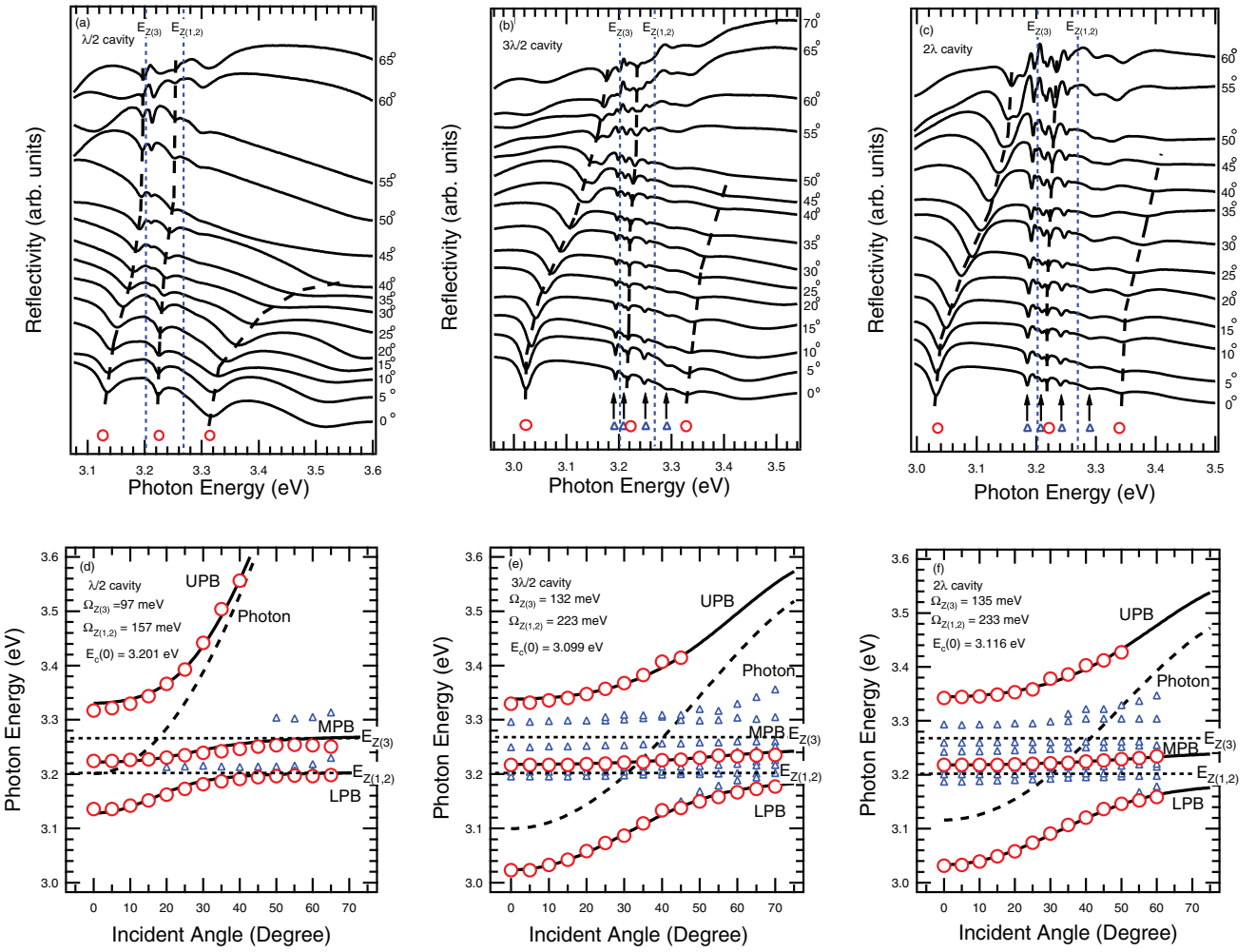

FIG. 3. (Color online) Angle-resolved reflectance spectra of the CuCl microcavities with the active-layer thicknesses of (a) $\lambda/2$, (b) $3\lambda/2$, and (c) 2λ. The open circles and triangles indicate the strongly coupled modes and weakly coupled modes, respectively. Incident-angle dependence of the cavity-polariton energies obtained in the respective CuCl microcavities with the active-layer thicknesses of (d) $\lambda/2$, (e) $3\lambda/2$, and (f) 2λ. The open circles and triangles are the energy positions of the strongly coupled modes and weakly coupled modes, respectively. The solid lines indicate the dispersion relationships of the cavity-polariton modes of the LPB, MPB, and UPB calculated from Eq. (2). The dotted lines indicate the Z_3 ($Z_{1,2}$) exciton energies, and the dashed curves show the dispersion relationship of the cavity photon.

by the ellipsometry measurements, was included within the range of about 10%. The ideal refractive index profile of the λ-cavity structure is shown in Fig. 1. The intensity profile of the electric field, $|E|^2$, along the growth direction at the normal incidence was calculated for the 387 nm wavelength using the conventional transfer-matrix method. In the λ cavity, the electric-field intensity has antinodes at the boundaries between the active layer and the DBRs, which indicates a loop cavity. The angle-resolved reflectance spectra were observed at 13 K using a 32 cm single monochromator combined with a charge coupled device (CCD) camera, where the spectral resolution was 0.37 nm. The probe light source was a Xe lamp. The spectroscopic ellipsometry measurements were carried out in order to characterize the refractive indices of the constituent layers and boundary regions between the constituent layers in the microcavities. The complex pseudodielectric functions were obtained by measuring the ellipsometric data at room temperature in the spectral range from 0.75 to 3.85 eV with a step of 0.02 eV at the incident angle of 65° using a spectroscopic phase-modulated ellipsometer (HORIBA Jobin-Ybon, UVISEL-9017TK).[17–19]

III. RESULTS AND DISCUSSION

The reflectance spectra of the λ cavity at various incident angles from 0° to 65° are shown in Fig. 2(a). The dashed vertical lines denote the energies of the Z_3 and $Z_{1,2}$ excitons: $E_{Z(3)} = 3.202$ and $E_{Z(1,2)} = 3.268$ eV, respectively. Many dip structures were observed in each reflectance spectrum. The three dips, marked with the open circles, clearly depend on the incident angle; however, the other dips, marked with the open triangles change only slightly with the incident angle. The strong angle-dependent dips originate from the cavity-polariton modes, which are assigned to be the lower polariton branch (LPB), the middle polariton branch (MPB), and the upper polariton branch (UPB) determined by the energy order.

The other dips are attributed to the weakly coupled modes that are discussed in previous reports.[12,20–22]

The energy positions of the dips observed in the angle-resolved reflectance spectra were plotted as a function of the incident angle, as shown in Fig. 2(b). The open circles and triangles show the cavity-polariton and weakly coupled modes, respectively. The energy positions of the Z_3 and $Z_{1,2}$ excitons are represented by the horizontal dotted lines. The dashed curve indicates the dispersion relationship of the cavity photon given by

$$E_{\rm cav}(\theta) = E_{\rm cav}(0)\left(1 - \frac{\sin^2\theta}{n_{\rm eff}^2}\right)^{-\frac{1}{2}}, \qquad (1)$$

where $E_{\rm cav}(0)$ is the energy of the cavity photon at the incident angle of $\theta = 0^\circ$ and $n_{\rm eff}$ is the effective refractive index of the active layer. To evaluate the vacuum Rabi splitting energies from the incident-angle dependence of the cavity-polariton modes, the eigenenergies of the cavity polaritons were calculated using the phenomenological Hamiltonian. The interaction between the cavity photon and the two states of the Z_3 and $Z_{1,2}$ excitons is given by the following matrix:[23]

$$H = \begin{pmatrix} E_{\rm cav}(\theta) & \frac{\Omega_{Z(3)}}{2} & \frac{\Omega_{Z(1,2)}}{2} \\ \frac{\Omega_{Z(3)}}{2} & E_{Z(3)} & 0 \\ \frac{\Omega_{Z(1,2)}}{2} & 0 & E_{Z(1,2)} \end{pmatrix}, \qquad (2)$$

where $\Omega_{Z(3)}$ and $\Omega_{Z(1,2)}$ are the coupling constants known as the vacuum Rabi splitting energies for the Z_3 and $Z_{1,2}$ excitons, respectively. The three solid curves, shown in Fig. 2(b), are the dispersion relationships of the cavity polariton fitted to the experimental results using Eq. (2). The fitted dispersion curves agree with the experimental results. Here, the effective refractive index of the active layer, $n_{\rm eff}$, is adopted as an adjustable parameter to the incident-angle dependence of the cavity-polariton modes, since the electric field of the cavity photon in the microcavities penetrates into the DBRs, as shown in Fig. 1. The value of $n_{\rm eff}$ is estimated to be 2.07 by fitting to the incident-angle dependence. Moreover, the evaluated Rabi splitting energies $\Omega_{Z(3)}$ and $\Omega_{Z(1,2)}$ are 110 and 195 meV, respectively. These Rabi splitting energies are larger than those obtained from the CuCl microcavities with the $PbBr_2/PbF_2$ DBRs.[12] It was noted that the large Rabi splitting energy were obtained by improving the crystal quality of the CuCl layer in our microcavities with the $PbCl_2$/NaF DBRs, and the confinement of the photon in the CuCl microcavities with the $PbCl_2$/NaF DBRs is stronger than that with the $PbBr_2/PbF_2$ DBRs, due to the high contrast of the refractive index between the $PbCl_2$ and NaF layers.

The reflectance spectra of the $\lambda/2$, $3\lambda/2$, and 2λ cavities observed at the various incident angles and the incident-angle dependence of the dip energies are shown in Fig. 3. The Rabi splitting energies in the $\lambda/2$, $3\lambda/2$, and 2λ cavities were estimated using the same method as mentioned above. All the fitted dispersion curves of the cavity polariton are in good agreement with the experimental results. The obtained Rabi splitting energies and the effective refractive indices are listed in Table I. As the active layer of the cavity becomes thicker, the Rabi splitting energies also increase. This means that the thicker active layers produce the wider coupling regions for the exciton and cavity photon. The variation of the Rabi splitting energy with the thickness of the active layer is roughly consistent with the result obtained in the quantum-well microcavities.[22,24] The Rabi splitting energy in the quantum-well microcavities has a square root dependence on $d/L_{\rm eff}$,[23,24] where d and $L_{\rm eff}$ are the active-layer thickness and the effective cavity thickness, respectively. Moreover, the Rabi splitting energies $\Omega_{Z(3)}$ and $\Omega_{Z(1,2)}$ vary from 97 to 135 meV and 157 to 233 meV, respectively. These variations demonstrate that the Rabi splitting energies are easily controlled in the splitting energy region above about 100 meV by changing the active-layer thickness, and the control range of the Rabi splitting energy in the high-energy region is larger than that reported in the ZnO microcavities.[25] In the present CuCl microcavities, because the Bohr radius of the exciton in CuCl is approximately 0.7 nm,[26] the center-of-mass motion of the CuCl exciton will be confined in the active layer.[27] The variation of the Rabi splitting energy will be explained by taking account of the overlap between the electric field of the cavity photon in the microcavity and the confined excitonic wave functions with various quantum numbers ($n \geqslant 1$) in the active layer, on the basis of the nonlocal response theory described later.[20] Moreover, when the thickness of the active layer is extremely thick, we expect that the optical properties will be close to those of bulk CuCl, as reported in Ref. 24.

TABLE I. Rabi splitting energies, $E_{\rm cav}(0)$ and $n_{\rm eff}$, estimated in the microcavities with various active-layer thicknesses, $L_{\rm cav}$.

$L_{\rm cav}$	$\Omega_{Z(3)}$ (meV)	$\Omega_{Z(1,2)}$ (meV)	$E_{\rm cav}(0)$ (eV)	$n_{\rm eff}$
$1/2\lambda$	97	157	3.201	1.52
λ	110	195	3.222	2.07
$3/2\lambda$	132	223	3.099	2.07
2λ	135	233	3.116	2.19

The reflectance spectrum of the λ cavity observed at the normal incidence in Fig. 4 shows not only the cavity-polariton modes with the large Rabi splitting energies, but also the weakly coupled modes. The observations of the

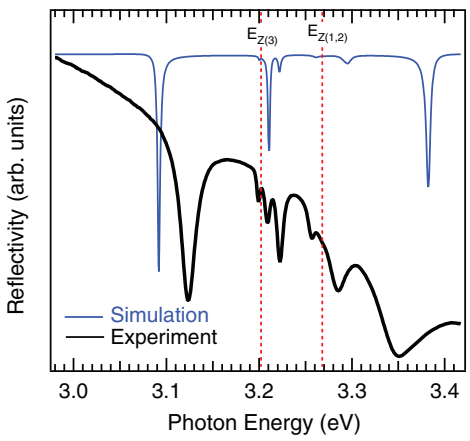

FIG. 4. (Color online) Experimental (black thick line) and calculated (blue thin line) reflectance spectra for the λ cavity at the normal incidence. The vertical dotted lines indicate the energy positions of the Z_3 and the $Z_{1,2}$ excitons of the CuCl active layer.

cavity-polariton and weakly coupled modes will originate from the coupling between the cavity photons and excitons with $n \geqslant 1$.[12,20] The coupling strength is represented by the overlap integral between the electric field of the cavity photon in the microcavity and the excitonic wave functions with $n \geqslant 1$ confined in the active layer,[24] which affects the reflectance spectra of the microcavities. Because the electric field of the cavity photon has the spatial variation as shown in Fig. 1, the long-wavelength approximation will not be adequate to calculate the reflectance spectra of the microcavities. Therefore, under the calculation of the reflectance spectra of the CuCl microcavities, we adopted the nonlocal response theory[28–30] and compared the calculated reflectance spectra with the observed ones at the normal incidence. The nonlocal response theory is appropriate for calculating the optical spectra when the spatial variation of the electric field cannot be neglected in the coherent region of the excitonic wave functions. The nonlocality is incorporated in the theory through the nonlocal susceptibility in the constitutive equation bridging the response between the electromagnetic wave and the spatially extended excitonic polarizations.[28] The induced polarization in the electric field $\boldsymbol{E}(\boldsymbol{r},\omega)$ under the linear response $\boldsymbol{P}_{\rm ex}(\boldsymbol{r},\omega)$ is

$$\boldsymbol{P}_{\rm ex}(\boldsymbol{r},\omega) = \epsilon_0 \int d\boldsymbol{r}' \boldsymbol{\chi}_{\rm ex}(\boldsymbol{r},\boldsymbol{r}',\omega) \cdot \boldsymbol{E}(\boldsymbol{r}',\omega), \tag{3}$$

where $\boldsymbol{\chi}_{\rm ex}(\boldsymbol{r},\boldsymbol{r}',\omega)$ is the nonlocal susceptibility written by

$$\boldsymbol{\chi}_{\rm ex}(\boldsymbol{r},\boldsymbol{r}',\omega) = \frac{1}{\epsilon_0} \sum_{\mu} \frac{\boldsymbol{\mathcal{P}}_{\mu}(\boldsymbol{r})\boldsymbol{\mathcal{P}}^{*}_{\mu}(\boldsymbol{r}')}{\hbar\omega_{\mu} - \hbar\omega - i\gamma_{\mu}} \tag{4}$$

in the rotating-wave approximations, where $\hbar\omega_{\mu}$, and γ_{μ} are the eigenenergy and the damping of the μth excitonic state, and $\boldsymbol{\mathcal{P}}_{\mu}(\boldsymbol{r})$ is the corresponding excitonic polarization represented by

$$\boldsymbol{P}_{\rm ex}(\boldsymbol{r},\omega) = \sum_{\mu} \boldsymbol{\mathcal{P}}_{\mu}(\boldsymbol{r}) b_{\mu}(\omega). \tag{5}$$

In this expression, $b_{\mu}(\omega)$ is the second-quantized annihilation exciton operator. The electric field $\boldsymbol{E}(\boldsymbol{r}',\omega)$ is

$$\boldsymbol{E}(\boldsymbol{r}',\omega) = \boldsymbol{E}_0(\boldsymbol{r}',\omega) + \mu_0\omega^2 \int d\boldsymbol{r}' \boldsymbol{G}(\boldsymbol{r},\boldsymbol{r}',\omega) \cdot \boldsymbol{P}_{\rm ex}(\boldsymbol{r}',\omega), \tag{6}$$

where $\boldsymbol{E}_0(\boldsymbol{r}',\omega)$ is the background electric field and $\boldsymbol{G}(\boldsymbol{r},\boldsymbol{r}',\omega)$ is the Green's function propagating both the transverse and longitudinal fields. The equation of motion for $b_{\mu}(\omega)$ is

$$(\hbar\omega_{\mu} - \hbar\omega - i\gamma_{\mu}) b_{\mu}(\omega) = \int d\boldsymbol{r}' \boldsymbol{\mathcal{P}}^{*}_{\mu}(\boldsymbol{r}) \cdot \boldsymbol{E}(\boldsymbol{r}',\omega). \tag{7}$$

Then, by substituting Eq. (6) into Eq. (7), the self-consistent equation is obtained as

$$\sum_{\mu} S_{\mu,\mu'} b_{\mu'}(\omega) = (\hbar\omega_{\mu} - \hbar\omega - i\gamma_{\mu}) b^{(0)}_{\mu}(\omega), \tag{8}$$

$$S_{\mu,\mu'}(\omega) \equiv (\hbar\omega_{\mu} - \hbar\omega - i\gamma_{\mu})\delta_{\mu,\mu'} + A_{\mu,\mu'}(\omega), \tag{9}$$

where $A_{\mu,\mu'}(\omega)$ means the interaction term between the induced excitonic polarizations via the Green's function,

$$A_{\mu,\mu'}(\omega) \equiv -\mu_0\omega^2 \int d\boldsymbol{r} \int d\boldsymbol{r}' \boldsymbol{\mathcal{P}}^{*}_{\mu}(\boldsymbol{r}) \cdot \boldsymbol{G}(\boldsymbol{r},\boldsymbol{r}',\omega) \cdot \boldsymbol{\mathcal{P}}_{\mu'}(\boldsymbol{r}'). \tag{10}$$

$b^{(0)}_{\mu}(\omega)$ is the exciton operator induced by the background field. $A_{\mu,\mu'}(\omega)$ contains the information on the spatial structures of the excitonic wave functions through $\boldsymbol{\mathcal{P}}_{\mu}(\boldsymbol{r})$ and on that of the electric field in the multilayered structure through the dyadic Green's function, as discussed in Ref. 31. In the calculation of the reflectance spectrum of the microcavity, the nonlocal response theory is applied to only the active layer of CuCl, because $PbCl_2$, NaF, and the substrate have no nonlocal susceptibilities. The reflectance spectrum of the λ cavity with the ideal refractive index profile shown in Fig. 1 has been calculated using Eq. (8), as shown in Fig. 4. In this calculation, the reflectance spectrum is calculated by using no fitting parameters, but by using the splitting energies of the longitudinal and transverse excitons in CuCl reported in Ref. 32 and the respective refractive indices of the constituent layers obtained by the ellipsometry measurements. Although the calculated reflectance spectrum shows the cavity-polariton and weakly coupled modes, the peak energies and spectral profiles of these modes deviate from the experimental results.

For the reflectance spectrum calculation based on the nonlocal response theory, we assumed that the microcavity has the ideal refractive index profile. This assumption leads to the deviation between the calculated and observed reflectance spectra. That is, the deviation will originate from the spatial fluctuation in the refractive index profile of the microcavity structure. The spatial fluctuation in the refractive index profile will reduce the confinement of the photon in the cavity and decrease the interaction region between the exciton and the photon. Therefore, in order to reveal the fluctuation in the refractive index profile of the cavity structure, we have characterized the refractive indices of the constituent layers and the interfaces between the layers using spectroscopic ellipsometry. The sample was a double layer consisting of $PbCl_2$ and NaF grown on the sapphire substrate. The designed thicknesses of the $PbCl_2$ and NaF layers were 200 nm. The complex pseudodielectric functions of the $PbCl_2$/NaF double layer were obtained in the transparent region to $PbCl_2$ and NaF from 0.75 to 3.85 eV. In Fig. 5(a), the energy dependence of the real and imaginary parts of the pseudodielectric functions $\mathrm{Re}\langle\epsilon\rangle$ (black circles) and $\mathrm{Im}\langle\epsilon\rangle$ (red squares) for the $PbCl_2$ /NaF double layer is shown. In the observed pseudodielectric functions, the smooth oscillatory structures in the whole energy range are the interference fringes in the sample. The pseudodielectric functions were fitted by taking account of the interference effect and by using the two complex refractive indices of $PbCl_2$ and NaF, where it is assumed that the $PbCl_2$/NaF double layer has an ideal structure without the imperfections around the interface between the $PbCl_2$ and NaF layers, as shown in the upper side of Fig. 5(b). The broken curves in Fig. 5(a) are the fitted pseudodielectric functions, which deviate from the experimental results. The deviation results from the imperfection of the sample structure around the

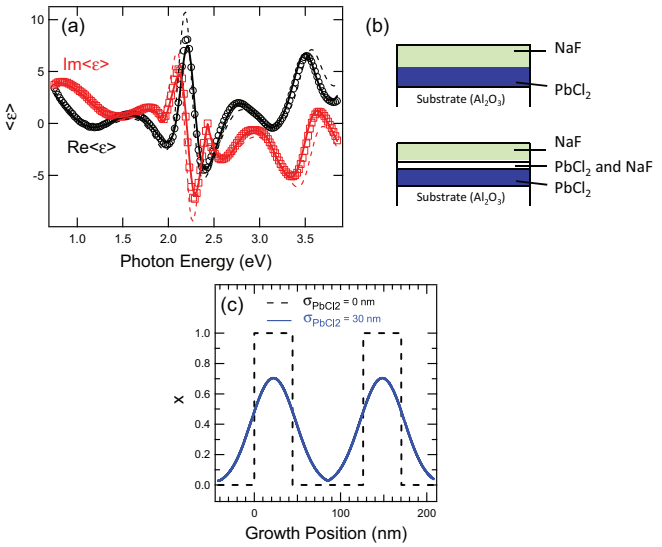

FIG. 5. (Color online) (a) Energy dependence of real and imaginary parts of the pseudodielectric function $\mathrm{Re}\langle\epsilon\rangle$ (black circles) and $\mathrm{Im}\langle\epsilon\rangle$ (red squares) for the $PbCl_2$/NaF double layer obtained by spectroscopic ellipsometry. The dashed and solid lines are the fitting results by assuming that the $PbCl_2$/NaF double layer has a structure without and with the intermediate layer around the interface between the $PbCl_2$ and NaF layers, respectively. (b) Schematic diagrams of the $PbCl_2$/NaF double layer without and with the intermediate layer. (c) Volume ratios of $PbCl_2$ and NaF as a function of growth position, $(PbCl_2)_x(NaF)_{1-x}$, in the $PbCl_2$/NaF DBR layers with the fluctuation width of $\sigma_{PbCl_2} = 30$ nm (solid line) and without the fluctuation (dashed line).

interfaces between the $PbCl_2$ and NaF layers. Therefore, the observed pseudodielectric functions were fitted by inserting the intermediate layer around the interface between the $PbCl_2$ and NaF layers shown in the lower side of Fig. 5(b). Here, we assume that the refractive index profile in the intermediate layer continuously changes between the refractive indices of the $PbCl_2$ and NaF layers, as described later. The solid curves in Fig. 5(a) are the fitted pseudodielectric functions obtained by inserting the intermediate layer, which are in good agreement with the experimental results. The fluctuation width, which corresponds to σ_A in Eq. (11) described later, of the intermediate layer around the interface was about 35 nm. The spectroscopic ellipsometry results for the $PbCl_2$/NaF double layer reveal that there are intermediate layers between the $PbCl_2$ and NaF layers. These intermediate layers are caused by mixed crystallization or the microscopic roughness of the interface. Therefore, the deviation between the calculated and observed reflectance spectra in Fig. 4 will be induced by the spatial fluctuations in the refractive indices around the interfaces between the constituent layers.

To determine the relationship between the reflectance spectra and the spatial fluctuation in the microcavity refractive index, we discuss the refractive index profile in the microcavity with the spatial fluctuation. First, we assume that the intermediate layers around the interfaces are constructed by mixing layers A and B (A: CuCl or $PbCl_2$; B: NaF) with the volume ratio x, namely $(A)_x(B)_{1-x}$. The volume ratio x continuously changes along the growth direction. This is represented by the convolution of the step function $\Theta(z)$ and the Gauss function $G(z,\sigma_A)$ as follows:

$$x(z) = \int dz' \Theta(z' \in A \text{ layer}) G(z',\sigma_A), \tag{11}$$

$$G(z,\sigma_A) = \frac{1}{\sqrt{\pi}\sigma_A} e^{-(z/\sigma_A)^2}, \tag{12}$$

where the parameter σ_A is the fluctuation width of the volume ratio. Figure 5(c) shows the spatial distribution of the $PbCl_2$/NaF volume ratio. The solid and dashed lines indicate the fluctuating $PbCl_2$/NaF layer and the ideal $PbCl_2$/NaF layer, respectively. Moreover, we define the refractive index profile along the cavity structure by using the effective-medium approximation (EMA).[33] The EMA shows that the effective dielectric constant of the mixed media can be calculated. The refractive index obtained using the EMA becomes n_A when the composite layer consists of only layer A ($x = 1$) or n_B when it consists of only layer B ($x = 0$). Accordingly, the refractive index of the composite layer takes values between n_A and n_B, depending on the volume ratio x. The calculated refractive index profiles of the λ cavity are shown in Figs. 6(a) and 6(b). The volume ratios of the DBRs and active layers have the various fluctuation widths of σ_{PbCl_2} and σ_{CuCl}, respectively. Under the above assumption, the normal-incident reflectance spectra of the microcavity with the spatial fluctuation have been calculated by using the nonlocal response theory. Figures 6(c) and 6(d) show the calculated reflectance spectra of the λ cavity for the Z_3 exciton at the various values of σ_{PbCl_2} for the DBR layer and σ_{CuCl} for the active layer, respectively. Here, the energy of the cavity photon is approximately equal to the resonant energy of the Z_3 exciton, and the damping constant of the Z_3 exciton in the CuCl layer is kept to 2 meV. Figure 6(c) shows that as σ_{PbCl_2} in the DBR layers becomes larger, which corresponds to the increase of the fluctuation in the DBR layer, the bandwidth of the stop band becomes narrower, and the full width at half-maximum (FWHM) of each dip becomes wider; that is, the Q factor becomes smaller with an increase in σ_{PbCl_2}. Moreover, the Rabi splitting energy becomes slightly smaller with the increasing fluctuation. This means that the fluctuation of the volume ratio in the DBRs tends to reduce the contrast of the refractive indices of the DBRs, and consequently the confinement of the photon in the microcavity is weakened due to the narrower stop band and the smaller reflectivity of the DBR. Figure 6(d) shows that as σ_{CuCl} becomes larger, the Rabi splitting energy reduces considerably, whereas the width of the stop band and Q factor change negligibly. The reason for this reduction of the Rabi splitting energy is that the coupling region between the photon and the exciton in the microcavity becomes smaller upon increasing the fluctuation.

The Q factors and Rabi splitting energies for the Z_3 and $Z_{1,2}$ excitons are plotted as a function of σ_A in Fig. 6(e) in order to clarify the effects of the spatial fluctuation on the Q factor and the Rabi splitting energies. The filled (open) circles show the variation in the calculated Q factor for the Z_3 ($Z_{1,2}$) exciton energy versus σ_{PbCl_2} in the empty cavity. The triangles and squares show the variations of the Rabi splitting energy for the Z_3 exciton versus σ_{PbCl_2} at the DBR and σ_{CuCl} at the active layer, respectively. The inverse triangles and diamonds are the variations in the Rabi splitting energy for the $Z_{1,2}$

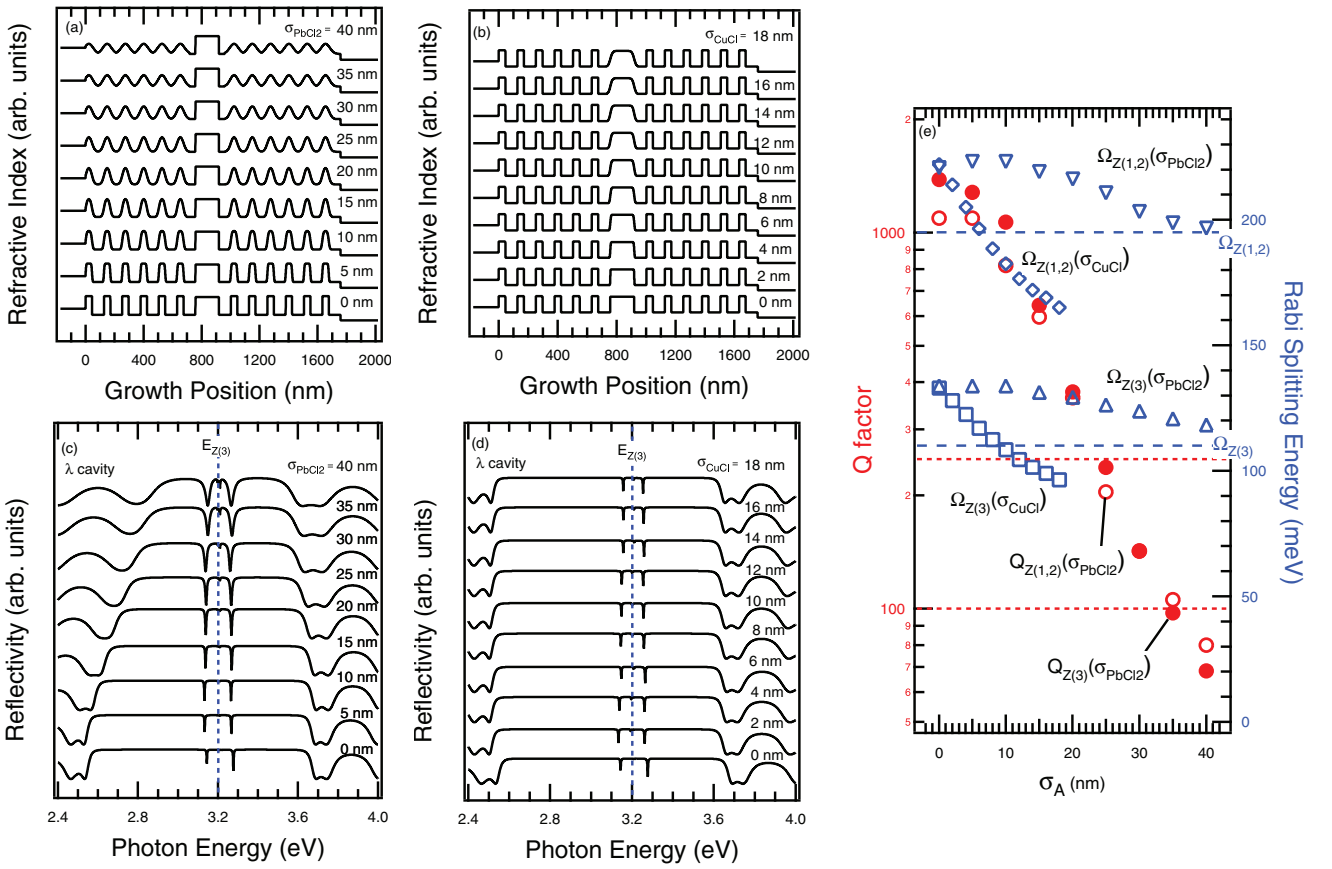

FIG. 6. (Color online) Calculated refractive index profiles in the λ cavities with various fluctuation widths of (a) σ_{PbCl_2} (b) and σ_{CuCl}. Calculated reflectance spectra for the Z_3 exciton in the λ cavities with various fluctuation widths of (c) σ_{PbCl_2} (d) and σ_{CuCl}. The vertical solid lines show the resonant energies of the Z_3 exciton. (e) Q factors and Rabi splitting energies as a function of σ_A obtained from the calculated reflectance spectra. The filled (open) circles show the σ_{PbCl_2} dependence of the Q factors at the Z_3 ($Z_{1,2}$) exciton energy. The triangles (squares) show the σ_{PbCl_2} (σ_{CuCl}) dependence of the Rabi splitting energy for the Z_3 exciton. Inverse triangles (diamonds) show the σ_{PbCl_2} (σ_{CuCl}) dependence of the Rabi splitting energy for the $Z_{1,2}$ exciton. The range of the Q factor shown by the horizontal dotted lines is estimated from the observed transmission spectra of the empty cavity. The dashed lines show the Rabi splitting energies for the Z_3 and $Z_{1,2}$ excitons obtained from the observed reflectance spectra of the λ cavity.

exciton versus σ_{PbCl_2} and σ_{CuCl}, respectively. It is obvious that the Q factor and the Rabi splitting energies were reduced with increasing σ_A. The Q factors are reduced from approximately 1000 to 100 as σ_{PbCl_2} increases from 0 to 40 nm. The increase of σ_{CuCl} reduces the Rabi splitting energies drastically, compared with the variation of the Rabi splitting energy versus σ_{PbCl_2}. This means that the fluctuation in the cavity layer dominantly affects the Rabi splitting energy.

Next, we estimated the fluctuation width σ_A in order to calculate the reflectance spectra of the fabricated microcavities with the fluctuations in the refractive index profiles of the cavity structures. As mentioned above, the Q factor for the empty cavity was experimentally estimated in the range of approximately 100–250, and the Rabi splitting energy for the Z_3 ($Z_{1,2}$) exciton in the λ cavity was 110 (195) meV, shown by the dashed line in Fig. 6(e). By comparing these experimental values with the calculated ones, the fluctuation width can be estimated to be $\sigma_{PbCl_2} = 30$ nm and $\sigma_{CuCl} = 6$ nm. The value of the fluctuation for the DBRs is consistent with the estimated value of the intermediate layer in the $PbCl_2$/NaF double layer using the spectroscopic ellipsometry.

The reflectance spectra of the microcavities with the fluctuation width σ_A at the normal incidence were calculated using the nonlocal response theory, and the dependence of the Rabi splitting energies on the active-layer thickness was obtained from the calculated reflectance spectra. The refractive index profiles with and without the fluctuations are shown by the solid and dashed lines in Fig. 7(a), respectively. In Fig. 7(b), the black thick lines indicate the observed reflectance spectra at the normal incidence, and the blue thin lines show the calculated results for each active-layer thickness. The dotted lines represent the calculated reflectance spectra of the empty cavities, which exhibit the cavity photon energies at 0°. In these calculations, as mentioned above, the calculated reflectance spectra on the basis of the nonlocal response theory are reproduced by using no fitting parameters, but by using the splitting energies of the longitudinal and transverse excitons in CuCl (Ref. 32) and the background dielectric constant of CuCl.[32] Moreover, the damping constants of the Z_3 and $Z_{1,2}$ excitons are 4 and 16 meV, respectively, estimated by the absorption spectra of the CuCl layer embedded between the two NaF layers. The arrows show the LPB, MPB, and UPB in

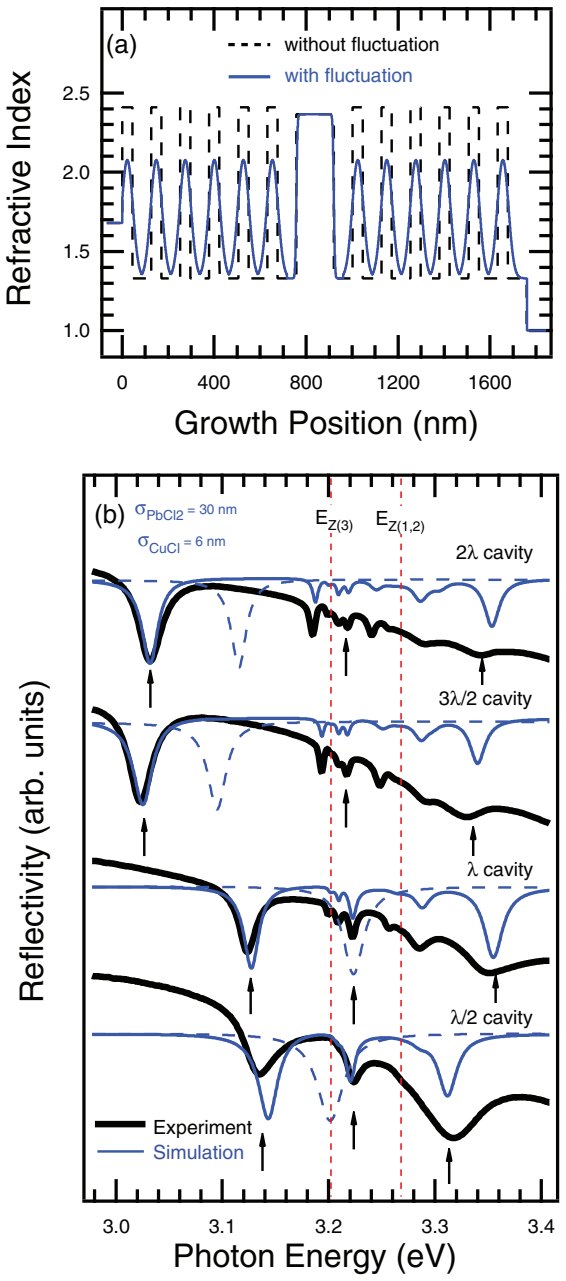

FIG. 7. (Color online) (a) Refractive index profiles of the cavity structures with and without the fluctuation width σ_A. The solid line shows the refractive index profile in the λ cavity with $\sigma_{PbCl_2} =$ 30 and $\sigma_{CuCl} = 6$ nm, and the dashed line shows that without the fluctuation ($\sigma_{PbCl_2} = 0$ and $\sigma_{CuCl} = 0$ nm). (b) Calculated and observed reflectance spectra of the microcavities with various active-layer thicknesses at the normal incidence, which are represented by thin blue and thick black lines, respectively. The dashed lines show the calculated reflectance spectra of the empty cavities, which show the cavity photon energies at normal incidence. The arrows indicate three polariton modes. The vertical dotted lines show the Z_3 and $Z_{1,2}$ exciton energies.

the energy order. The energy positions and the FWHMs of the cavity-polariton and weakly coupled modes observed from the calculated results are in good agreement with the experimental

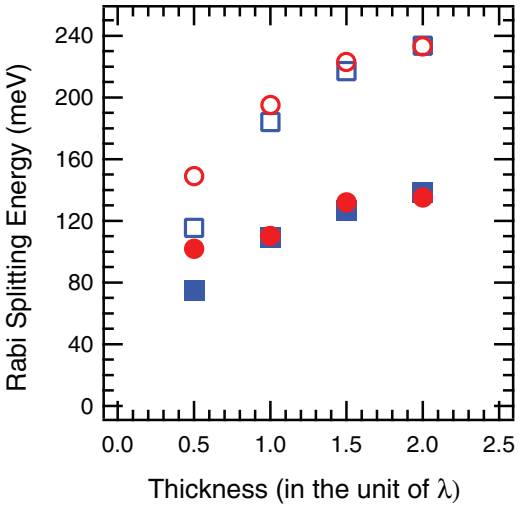

FIG. 8. (Color online) Active-layer-thickness dependence of the Rabi splitting energies obtained from the observed and calculated reflectance spectra. The filled and open circles indicate the Rabi splitting energies for the Z_3 and $Z_{1,2}$ excitons, respectively, obtained from the observed reflectance spectra of the microcavities with various active-layer thicknesses. The filled and open squares indicate the Rabi splitting energies for the Z_3 and $Z_{1,2}$ excitons, respectively, obtained from the calculated reflectance spectra.

results for the respective microcavities. For the higher-energy side near the UPB, the FWHM of the experimental spectra is wider than the calculated ones and the reflectivity of the experimental spectra is lower than the calculated ones because the exciton continuum state of CuCl exists around 3.4 eV. Figure 8 shows the Rabi splitting energies from the observed and calculated reflectance spectra of the microcavities with the various active-layer thicknesses. The Rabi splitting energies obtained from the calculated spectra agree well with the experimental results. This result shows that the exciton-photon strong interaction can be precisely controlled for the wide energy ranges. Thus, we demonstrated that the calculation method with the nonlocal response theory and the fluctuations in the refractive index profiles well reproduce the reflectance spectra and the Rabi splitting energies resulting from the interaction between the excitons and the cavity photon in the fabricated CuCl microcavity.

IV. CONCLUSION

We have investigated the optical property of the fabricated CuCl microcavities with the various active-layer thicknesses consisting of the $PbCl_2$/NaF DBRs with the Q factor of approximately 250. The three-polariton and the weakly coupled modes were observed in the angle-resolved reflectance spectra. The dispersion relationship of the polariton modes was represented by the phenomenological 3×3 Hamiltonian. These results indicate that the Rabi splitting energies are widely controlled by changing the active-layer thickness. The reflectance spectra of the CuCl microcavities with the fluctuations in the refractive index profiles of the cavity structures have been calculated using the nonlocal response theory, and the effect of the spatial fluctuations in the refractive index profiles on the Rabi splitting energies and the Q factor

has been demonstrated. The calculated reflectance spectra are in good agreement with the observed ones, which means that the disagreement between the experimental and calculated spectra reported in Ref. 12 originates from the fluctuations in the refractive index profiles of the microcavity structures. The good agreement between the calculated and observed spectra in this work demonstrates that the calculation method with the fluctuation and the nonlocal response theory is crucial to quantitatively reproduce the Rabi splitting energies and reflectance spectra caused by the interaction between the quantized exciton and photon, which is essentially important for engineering control of the Rabi splitting.

ACKNOWLEDGMENTS

This study was supported by the Japan Society for the Promotion of Science, KAKENHI Grants No. 23340087 and No. 24654090.

[1]C. Weisbuch, M. Nishioka, A. Ishikawa, and Y. Arakawa, Phys. Rev. Lett. **69**, 3314 (1992).
[2]J. Kasprzak, M. Richard, S. Kundermann, A. Baas, P. Jeambrun, J. M. J. Keeling, F. M. Marchetti, M. H. Szymańska, R. André, J. L. Staehli, V. Savona, P. B. Littlewood, B. Deveaud and Le Si Dang, Nature (London) **443**, 409 (2006).
[3]H. Deng, H. Haug, and Y. Yamamoto, Rev. Mod. Phys. **82**, 1489 (2010).
[4]P. G. Savvidis, J. J. Baumberg, R. M. Stevenson, M. S. Skolnick, D. M. Whittaker, and J. S. Roberts, Phys. Rev. Lett. **84**, 1547 (2000).
[5]D. Bajoni, P. Senellart, E. Wertz, I. Sagnes, A. Miard, A. Lemaître, and J. Bloch, Phys. Rev. Lett. **100**, 047401 (2008).
[6]J. Kasprzak, S. Reitzenstein, E. A. Muljarov, C. Kistner, C. Schneider, M. Strauss, S. Höfling, A. Forchel, and W. Langbein, Nat. Mater. **9**, 304 (2010).
[7]F. Médard, J. Zuniga-Perez, P. Disseix, M. Mihailovic, J. Leymarie, A. Vasson, F. Semond, E. Frayssinet, J. C. Moreno, M. Leroux, S. Faure, and T. Guillet, Phys. Rev. B **79**, 125302 (2009).
[8]T. Kawase, S. Komura, K. Miyazaki, D. Kim, and M. Nakayama, Physica E **42**, 2567 (2010).
[9]N. Antoine-Vincent, F. Natali, D. Byrne, A. Vasson, P. Disseix, J. Leymarie, M. Leroux, F. Semond, and J. Massies, Phys. Rev. B **68**, 153313 (2003).
[10]R. Butté, G. Christmann, E. Feltin, J.-F. Carlin, M. Mosca, M. Ilegems, and N. Grandjean, Phys. Rev. B **73**, 033315 (2006).
[11]H. Ishihara and K. Cho, Appl. Phys. Lett. **71**, 3036 (1997).
[12]G. Oohata, T. Nishioka, D. Kim, H. Ishihara, and M. Nakayama, Phys. Rev. B **78**, 233304 (2008).
[13]H. Ajiki and H. Ishihara, J. Phys. Soc. Jpn. **76**, 053401 (2007).
[14]H. Oka and H. Ishihara, Phys. Rev. Lett. **100**, 170505 (2008).
[15]M. Bamba and H. Ishihara, Phys. Rev. Lett. **105**, 123906 (2010).
[16]M. Nakayama, K. Miyazaki, T. Kawase, and D. Kim, Phys. Rev. B **83**, 075318 (2011).
[17]W. M. Duncan and S. A. Henck, Appl. Surf. Sci. **63**, 9 (1993).
[18]T. Holden, P. Ram, F. H. Pollak, J. L. Freeouf, B. X. Yang, and M. C. Tamargo, Phys. Rev. B **56**, 4037 (1997).
[19]D. E. Aspnes, in *Optical Properties of Solids: New Developments*, edited by B. O. Seraphin (North-Holland, New York, 1976), Chap. 15, pp. 800–846.
[20]M. Ichimiya, M. Ashida, H. Yasuda, H. Ishihara, and T. Itoh, Phys. Rev. Lett. **103**, 257401 (2009).
[21]H. Ishihara and J. Kishimoto, in *Proceedings of the 25th International Conference on the Physics of Semiconductors*, edited by N. Miura and T. Ando (Springer, Berlin, 2001), p. 685.
[22]Y. Chen, A. Tredicucci, and F. Bassani, Phys. Rev. B **52**, 1800 (1995).
[23]V. Savona, L. C. Andreani, P. Schwendimann, and A. Quatropani, Solid State Commun. **93**, 733 (1995).
[24]A. Tredicucci, Y. Chen, V. Pellegrini, M. Börger, L. Sorba, F. Beltram, and F. Bassani, Phys. Rev. Lett. **75**, 3906 (1995).
[25]T. Kawase, D. Kim, and M. Nakayama, Phys. Status Solidi C **9**, 1797 (2012).
[26]S. Lewonczuk, J. Ringeissen, and S. Nikitine, J. Phys. (Paris) **32**, 941 (1971).
[27]Z. K. Tang, A. Yanase, T. Yasui, Y. Segawa, and K. Cho, Phys. Rev. Lett. **71**, 1431 (1993).
[28]K. Cho, in *Optical Response of Nanostructures: Microscopic Nonlocal Theory* (Springer-Verlag, Berlin, 2007), Chaps. 1–4.
[29]M. Bamba and H. Ishihara, Phys. Rev. B **78**, 085109 (2008).
[30]T. Iida and H. Ishihara, Phys. Rev. B **77**, 245319 (2008).
[31]W. C. Chew, in *Waves and Fields in Inhomogeneous Media, IEEE Press Series on Electromagnetic Wave* (IEEE, New York, 1995).
[32]M. Ueta, H. Kanzaki, K. Kobayashi, Y. Toyozawa, and E. Hanamura, in *Excitonic Processes in Solids* (Springer-Verlag, Berlin, 1986), Chap. 3, p. 119.
[33]D. E. Aspnes, Thin Solid Films **89**, 249 (1982).